

Article

Laminar Structure and Reservoir Quality of Shales with High Clay Mineral Content in the Qingshankou Formation, Songliao Basin

Ganlin Hua ^{1,2} , Songtao Wu ^{2,*}, Jinyou Zhang ³, Rongchang Liu ², Modi Guan ², Yi Cai ², Mengying Li ² and Surong Zhang ²

¹ School of Energy Resource, China University of Geosciences (Beijing), Beijing 100083, China

² Research Institute of Petroleum Exploration and Development (RIPE), China National Petroleum Corporation (CNPC), Beijing 100083, China

³ Research Institute of Exploration and Development of Daqing Oilfield Company Ltd., Daqing 163000, China

* Correspondence: wust@petrochina.com

Abstract: This paper investigates high-maturity organic matter-rich shales with high clay mineral contents in the Qingshankou Formation, in the Gulong Depression of the Songliao Basin, at a sub-millimeter scale, using a new laminar division method based on XRF data. The influence of laminar structure on reservoir quality is examined using a combination of geochemistry, mineralogy, and pore structures. Explanatory models are established. Three types of laminar units are distinguished in the study area based on differences in pore structure. These are clay mineral laminae (UA), clay mineral-Ostracod laminae (UB), and clay mineral-felsic laminae (UC). UA has illite intergranular pores, micro-fractures, and organic pores, with diameters of 0.5–2 μm . UB primarily contains Ostracod shell margin fractures, pyrite intergranular pores, and chlorite intragranular pores. UC contains albite and illite intergranular pores. Nitrogen adsorption tests show that UA has the highest clay content and the best specific pore volume and specific surface area, indicating that clay minerals are the main contributors to the pores in this type of unit. 2D–3D models of different laminae reveal that carbonate cement is widely developed in UB and UC, but dissolution pores are less developed, with the result that the porosity of UA is two to three times greater than that of UB or UC. It appears that intergranular pores and fractures, formed during the transformation of clay minerals during the advanced thermal evolution stage, are the main contributors to storage space and flow channels. Thermal evolution, clay mineral transformation, and carbonate cementation are the key factors causing differences between laminar units. In addition, clay mineral laminae (UA) are the most important laminar units for shale oil enrichment in the study area. This finding is of great significance for accurately predicting the distribution of shale “sweet spots” and guiding shale oil and gas exploration.

Keywords: shale oil and gas; sub-millimeter-scale evaluation; reservoir property; laminar pattern



Citation: Hua, G.; Wu, S.; Zhang, J.; Liu, R.; Guan, M.; Cai, Y.; Li, M.; Zhang, S. Laminar Structure and Reservoir Quality of Shales with High Clay Mineral Content in the Qingshankou Formation, Songliao Basin. *Energies* **2022**, *15*, 6132. <https://doi.org/10.3390/en15176132>

Academic Editors: Shang Xu, Qiulei Guo and Feng Yang

Received: 14 July 2022

Accepted: 12 August 2022

Published: 24 August 2022

Publisher's Note: MDPI stays neutral with regard to jurisdictional claims in published maps and institutional affiliations.



Copyright: © 2022 by the authors. Licensee MDPI, Basel, Switzerland. This article is an open access article distributed under the terms and conditions of the Creative Commons Attribution (CC BY) license (<https://creativecommons.org/licenses/by/4.0/>).

1. Introduction

As one of the richest oil-bearing continental sandstone-type basins in the world, the Songliao Basin has made a significant contribution to the development of China's petroleum industry [1]. The oil from the shale of the Qingshankou Formation in the Gulong Depression of the Songliao Basin, with its high clay minerals content, is typical of China's continental shale oil [2]. Painstaking experiments, exploration, and research have revealed a full-concave overall oil-bearing structure with excellent resource potential [3]. Like the continental shales in other basins, the Gulong shales are characterized by fine grain sizes and multiple phase types, with frequent vertical variations and strong heterogeneity [4]. However, it should be noted that the Gulong shales differ significantly from the shales of North America and those of the Luchaogou Formation in the Jimsar Depression and the

Chang 7 section in the Ordos Basin in China. The Gulong shales are characterized by ‘three highs’: high clay mineral contents, high maturity, and high lamina density. Diverse types and complex assemblages of laminae are common in the formation, but their comparative influence on reservoir quality and the ‘sweet spot zone/section’ is unclear [5]. It is, therefore, important to study the shale laminae in the Qingshankou Formation of the Songliao Basin, and to generally improve the evaluation of high-maturity high-clay-mineral-content shale reservoirs, to facilitate stable shale oil production in the Gulong area.

In recent years, explorers and geologists have recognized the heterogeneity of shale [6] and its prevalent laminar structures [7]. They have also found that the hydrocarbon generation potential and reservoir physical properties of shale with lamina are significantly better than those of massive mudstone [4,8], which shows that lamina will have a significant impact on oil and gas production, storage, and production, and should be the focus of future research. Foreign scholars have studied the Banff and Exshaw Formations in the sedimentary basin of western Canada [9], the lower Cretaceous and Upper Cretaceous shales in the Denver Basin [10], the Mississippi Barnett shale in northern Texas [11] and the upper Jurassic Hainsville shale in eastern Texas and Western Louisiana [12] and found that silty sand laminae are widely developed in shale reservoirs, and silty sand laminae play an important role in the distribution of shale reservoirs. Domestic scholars Huang et al. confirmed that laminar development will play an important role in shale gas production through research on Yanchang Formation in Ordos Basin [13]. In addition, predecessors found that the spatial types and properties of reservoirs vary significantly with different laminae. Breyer found that the oil and gas production of Eagle Ford shale wells was positively correlated with the interbedding frequency of limestone and mudstone [14]; Zhao studied the carbonate lamina in Dongying sag of Bohai Bay Basin and believed that it was of great significance for paleoenvironment restoration and TOC response [15]; Xi discussed different laminar units in the Yanchang Formation and concluded that the reservoir space of felsic lamina in the Ordos Basin was the best [16], indicating that laminae lead to heterogeneity and differences in reservoir “sweet spot” distribution. Therefore, the differences between different laminae should be paid more attention, to understand the relationship between different types of laminae and organic matter enrichment, reservoir space, and hydrocarbon production.

However, the published literature mainly focuses on the macroscopic heterogeneity of shale—at the decimeter and meter scales of shale facies—using petrological, mineralogical, geochemical, reservoir, and oil-bearing analyses of whole cores. Therefore, the results represent a composite of multiple lamina combinations and do not reveal the different influences of specific types of the lamina on the quality of the shale. At the same time, due to the complexity of laminar structure and the limitation of analysis methods, the diversity of mineral composition, pore structure, and organic geochemical characteristics of different laminae have largely been ignored by previous studies. For example, analyzing the same core at a centimeter or meter scale using random sampling locations will lead to huge variations in the data. Since it is difficult to guarantee the same sampling locations for different experiments, it is difficult to ensure matching of the results of different experiments in the fine evaluation of the lamina, reducing the credibility of reservoir evaluation. It is difficult to distinguish differences in the chemical compositions of black shales with the naked eye, so a great deal of time and experimental effort is required to classify laminae.

In this paper, to address this problem, the high-clay mineral shale of the Cretaceous Qingshankou Formation is used as an example to accurately distinguish different laminar units using in situ high-resolution X-ray fluorescence spectroscopy (XRF) and wire-cutting methods. Rapid and fine imaging of elements at a micrometer scale provides a basis for millimeter-scale examination and description of shale laminae. The experimental analysis process is also optimized. Before high-resolution non-destructive imaging was carried out and the laminar units were divided, the samples were crushed to minimize the influence of heterogeneity of samples along the laminar direction and to ensure the homogeneity of samples for field emission scanning electron microscopy (FE-SEM), rock

pyrolysis, total organic carbon (TOC), X-ray diffraction mineral analysis (XRD), nano-CT, nitrogen adsorption, and other experiments. By comparing the mineral compositions, geochemical characteristics, and reservoir space characteristics of different laminae in high-clay mineral shales, the influence of laminar structure on shale reservoir quality is explored, and the dominant types of lamina units and space characteristics are identified, providing a scientific basis for understanding the oil enrichment mechanism of the shale in the Qingshankou Formation and guiding ‘sweet-spot’ selection.

2. Geological Setting

The Gulong Depression is located in the western part of the central depression in the Songliao Basin [17] (Figure 1a), covering an area of about 3700 km². The Qingshankou Formation is the main hydrocarbon source in the depression and is divided vertically into three sections. The Qing One Section is the main shale oil section [18], with an average thickness of 61.5 m [19]. Its average TOC content is 1.9%, and Ro values are 0.70%~1.13% [18]. The Qingshankou shales are generally mature. Large-scale water incursion occurred in the basin during the depositional period, and the lithology is mainly black and grey shales interbedded with oil shales, thinly bedded mesomorphic tuffs, and a few thinly bedded siltstones, rich in fossil fauna of multiple phylae including mesomorphs, lobate limbs, and bivalves [20]. Interventional studies involving animals or humans, and other studies that require ethical approval, must list the authority that provided approval and the corresponding ethical approval code.

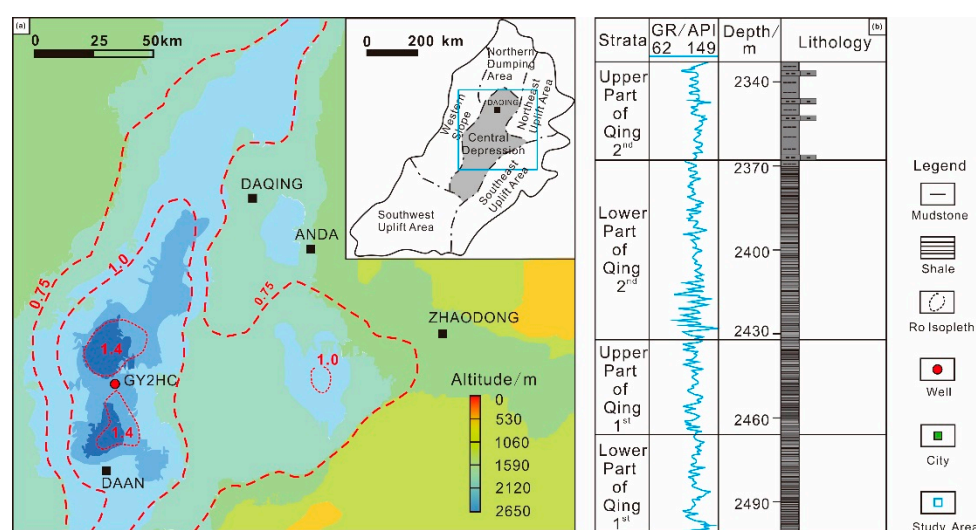


Figure 1. Geological overview of the study area. (a) Tectonic unit of the Songliao Basin and the location of the study area; (b) lithological column map of the Gulong 3HC well logs [2].

3. Experimental Samples and Methods

3.1. Fine Division of the Laminar Units

In this paper, a full-diameter black organic-rich high-clay-mineral core sample was collected from well GY2HC (indicated by the red dot in Figure 1a), with a length of 17 cm and a diameter of 10 cm. First, the sample was cut into two parts, perpendicular to the laminar direction at about one-third of the diameter, and trimmed to obtain a rectangular piece for XRF scanning. The flat surface of the rectangular piece was examined under an M4 Tornado high-performance micro-area X-ray fluorescence spectrometer to obtain the longitudinal lamina characteristics and element distribution. The scan step was 20 µm and the energy was 40 keV. The XRD results and the longitudinal elements of XRF confirmed the main mineral types in the study area (illite, quartz, feldspar, carbonate minerals, and pyrite) and the corresponding key elements (Ca, Fe, Si, K, Mg and Al). Combining the elements Al, Mg, K, Na and Si yielded a pink, mixed-blue XRF image that confirms that the

developmental background of the sample is clay minerals (Figure 2b). Furthermore, Ca and Fe, which vary significantly in the longitudinal direction, were rendered as red and yellow stripes to identify Ostracod laminae (Figure 2c,d) and the XRF sample was prepared into rock thin sections to identify felsic lamina (Figure 2a). A lamina division scheme for the Gulong organic-rich shale was established, with three distinct units: UA (clay mineral laminae), UB (clay mineral-Ostracod laminae), and UC (clay mineral-felsic laminae). The remaining column samples were cut parallel to the laminar direction to obtain 32 single lamina samples, which were then subjected to secondary testing.

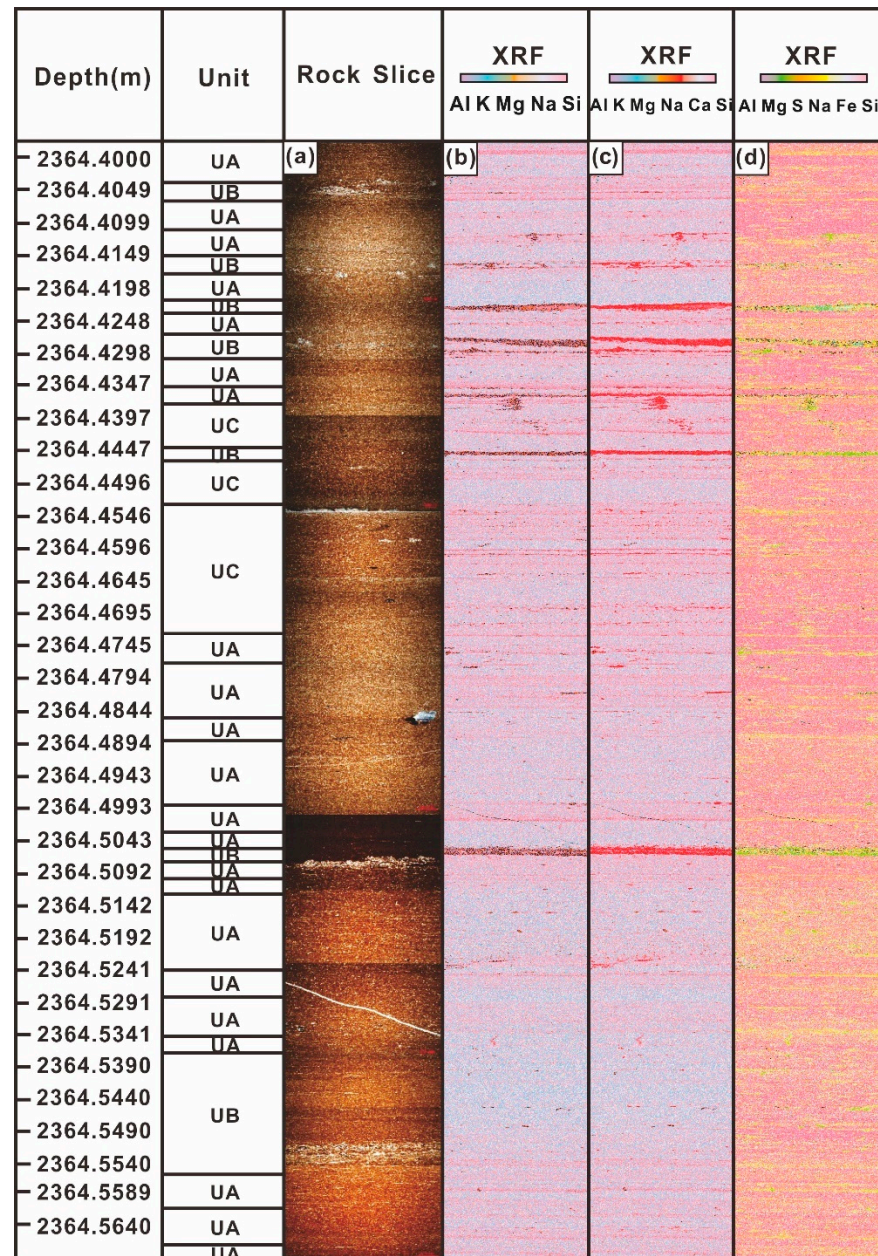


Figure 2. Laminae division based on XRF and rock thin section.

3.2. Key Experimental Analyses

Mineralogical compositions, chemical compositions and pore structure data in Table 1 were carried out simultaneously by XRD, ROCK-EVAL, nano-CT, NMR (nuclear magnetic resonance spectroscopy) and cyro-focused ion beam scanning electron microscopy (FIB-SEM). Rock thin section, FE-SEM, FIB-SEM, QEMSCAN, TOC, ROCK-EVAL, XRD,

and nano-CT were all carried out in the laboratory of the National Energy Tight Oil and Gas Research and Development Center. Low-temperature nitrogen adsorption tests were performed at Peking University. TOC and rock pyrolysis were analyzed using a CS-i carbon and sulfur analyzer and Rock-Eval 6 on 200 mesh samples based on the standards “Determination of Total Organic Carbon in Sedimentary Rocks” [21] and “Rock Pyrolysis Analysis” [22]. Rock mineral compositions were analyzed using a Rigaku-2500 radiographic diffractometer at an operating voltage of 45 kV and a current of 150 mA. The experiments were carried out following the standard “Method for the X-ray Diffraction Analysis of Clay Minerals and Common Non-Clay Minerals in Sedimentary Rocks” [23]. Mineral morphology was analyzed using a QUANTA FEG 450 for point-by-point energy spectroscopy of the samples at a resolution of 1 μm [24], combined with Apreo high-resolution field emission scanning electron microscopy. Inorganic and organic pores were scanned layer by layer using an UltraXRM-L200 and a Helios NanoLab 650, respectively. After the image was acquired, Avizo Fire software was used to reconstruct the 3D model and calculate the porosity following the oil and gas industry standard “Rock 3D pore structure determination method Part 1: CT scanning method, SY/T7410.1-2018” [25]. The nitrogen adsorption experiments were carried out using a Micromeritics ASAP 2020 specific surface area analyzer from the USA. The test temperature was that of liquid nitrogen (77.35 K) and the relative pressure P/P_0 ranged from 0.005 to 1.0.

Table 1. Chemical compositions, mineral compositions, and pore structure data for the 32 samples.

Sample	Depth (m)	XRD Mineral Composition (%)							ROCK-EVALChemical Composition			Nitrogen Adsorption Experiment			Nano CT	NMR	FIB-SEM
		Quartz	Feldspar	Calcite	Pyrite	Illite/Smectite Mixed Layer	Illite	Chlorite	TOC (%)	S1 (mg/g)	S2 (mg/g)	Average Diameter (Å)	BET Surface Area(m ² /g)	BJH Pore Volume (cm ³ /g)	Porosity (%)	Porosity (%)	Porosity (%)
1	2364.4000	36.2	7	1.8	3.8	17.92	29.184	4.096	2.30	3.02	3.73	182.7674	23.9111	0.109868			
2	2364.4049	37.2	7	1.6	3.2	18.36	27.54	5.1	2.34	2.98	4.75	198.9769	24.8854	0.124393			
3	2364.4099	33.2	6.5	2.3	4.4	20.368	28.408	4.824	2.34	3.23	2.96						
4	2364.4110	32.7	5.6	2.5	5.1	18.935	31.378	3.787	2.11	2.70	2.47	192.1353	26.2548	0.126762	0.84	0.81	0.4
5	2364.4160	35.3	5.9	4.3	5.2	15.283	28.594	5.423	2.06	2.54	2.59						
6	2364.4198	29.5	6.1	1.5	5.5	18.942	34.44	4.018	2.12	2.78	2.99						
7	2364.4210	32	5.8	5.4	4.2	21.566	26.826	4.208	2.07	2.55	2.61						
8	2364.4248	31.9	5.6	2.7	4.5	18.249	31.521	5.53	2.14	2.85	2.98						
9	2364.4298	34.4	7.6	4	3.9	20.541	25.05	4.509	2.48	3.27	3.54	197.5474	20.9797	0.104142	0.32		
10	2364.4300	32.7	6.9	3.1	2.8	20.71	29.975	3.815	2.40	3.46	3.47	191.2211	22.0494	0.105993		0.91	
11	2364.4360	35.4	4.1	4	2	15.805	33.245	5.45	2.25	3.12	3.48						
12	2364.4400	36.3	6	2.4	4.1	16.384	30.72	4.096	2.27	3.31	3.22	191.78	20.9594	0.101030			
13	2364.4447	28.6	6.3	13.8	10.2	13.152	23.427	4.521	2.11	2.85	2.47	189.1186	19.2355	0.091492	0.85		0.83
14	2364.4496	35.5	6	2.3	5	16.896	30.208	4.096	2.30	3.37	3.74						
15	2364.4645	34.8	7.1	3.1	3.5	20.6	26.78	4.12	2.25	3.13	3.38	163.7265	17.9416	0.073773	0.69	0.94	0.31
16	2364.4745	33	6.5	1.8	3.9	17.536	33.428	3.836	2.47	3.57	3.51	183.1044	22.6552	0.104323		0.97	
17	2364.4800	33.4	6.6	0.6	4.8	19.656	31.122	3.822	2.16	3.35	3.20	219.8406	17.8862	0.098721			
18	2364.4850	32.6	7	0.8	4.5	13.775	36.366	4.959	2.02	3.10	3.03						
19	2364.4943	31.4	6.3	0.9	4.6	21.584	31.808	3.408	2.14	2.98	3.11					0.11	
20	2364.5000	33	4.9	1	2.7	18.104	35.624	4.672	2.03	3.05	2.99	194.8713	21.4165	0.10485		0.82	
21	2364.5043	29.3	6.6	3	4.2	21.053	31.295	4.552	1.99	2.88	2.66						
22	2364.5070	26.2	7.5	9.7	7.7	16.626	27.873	4.401	1.88	2.80	2.64						
23	2364.5092	32.4	6.8	1.5	4.3	17.6	33	4.4	1.87	2.72	2.35						
24	2364.5110	35.8	7.6	2.5	6.1	14.88	29.76	3.36	1.90	2.60	2.72						
25	2364.5192	31.5	6.5	2.9	5.4	18.795	31.146	3.759	2.12	3.02	2.96						
26	2364.5260	33	7.6	1	6.7	16.027	33.088	2.585	1.96	2.92	3.14						
27	2364.5300	28.9	6.2	2.4	6.4	20.196	33.099	2.805	1.97	2.84	2.91	171.5379	23.3542	0.100856		9.6	
28	2364.5370	28.1	5.9	1.5	4.5	24	33	3	1.96	3.02	3.05						
29	2364.5470	30.4	6.6	1.5	4.1	20.664	33.866	2.87	1.99	2.97	3.07						
30	2364.5589	33.3	6.1	2	4.7	19.404	31.262	3.234	1.90	2.85	3.05						
31	2364.5640	31.2	6.4	1.4	3.6	22.96	30.422	4.018	1.96	2.91	2.99						
32	2364.5700	31.1	5.7	0.7	4.3	23.28	31.428	3.492	1.88	2.80	2.64						

4. Types and Characteristics of Lamina Units

4.1. Clay Mineral Lamina Unit (UA)

UA is the predominant lamina type in the study area. The monopolar microscope shows that UA is uniformly brown in color (Figure 3a₁), developing weak horizontal bedding. The organic matter is generally yellowish brown–dark brown agglomerate, arranged in a parallelogrammatic orientation with the clay minerals and distributed independently and sporadically between the matrix minerals. SEM images show that the clay mineral laminae are dominated by illite, which accounts for approximately 50%. The laminae contain minor, sporadically developed minerals such as euhedral pyrite and calcite (Figure 3a₂). QEMSCAN and XRD results are consistent, showing clay minerals in UA are from a minimum at 48% to a maximum at 60%. UA develops approximately 38% quartz and feldspar, and less than 4% carbonate minerals. The S1 of the UA averages 6.005 mg/g and the highest TOC can be 2.47% (Table 1).

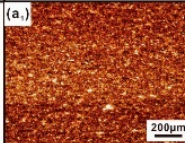
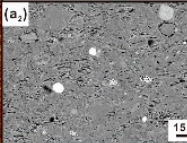









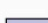


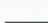

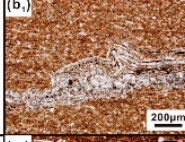
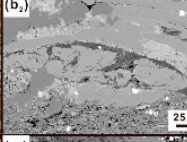
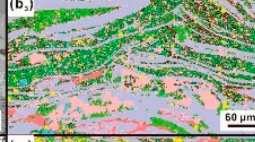
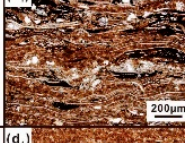
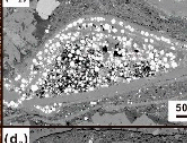

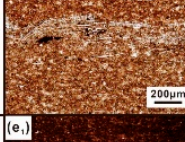

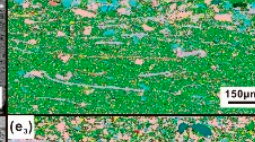



Laminar Units	Slice Characteristics	SEM Characteristics	Mineral Distribution (QEMSCAN)	Mineral Content (QEMSCAN)	Mineral Symbols																								
Clay Mineral Lamina	(a ₁) 	(a ₂) 	(a ₃) 	<table><tr><th>Mineral</th><th>Content/%</th><th>Mineral</th><th>Content/%</th></tr><tr><td>Illite</td><td>49.20</td><td>Chlorite</td><td>1.11</td></tr><tr><td>Quartz</td><td>32.50</td><td>Pores</td><td>0.95</td></tr><tr><td>Biotite</td><td>5.65</td><td>Smectite</td><td>0.67</td></tr><tr><td>Albite</td><td>5.09</td><td>Calcite</td><td>0.46</td></tr><tr><td>Pyrite</td><td>2.74</td><td>Others</td><td>1.63</td></tr></table>	Mineral	Content/%	Mineral	Content/%	Illite	49.20	Chlorite	1.11	Quartz	32.50	Pores	0.95	Biotite	5.65	Smectite	0.67	Albite	5.09	Calcite	0.46	Pyrite	2.74	Others	1.63	<div> Quartz</div> <div> Apatite</div> <div> Pyrite</div> <div> Chlorite</div> <div> Illite</div> <div> Smectite</div> <div> K-Feldspar</div> <div> Albite</div> <div> Calcite</div> <div> Gypsum</div> <div> Biotite</div> <div> Muscovite</div> <div> Pores</div>
Mineral	Content/%	Mineral	Content/%																										
Illite	49.20	Chlorite	1.11																										
Quartz	32.50	Pores	0.95																										
Biotite	5.65	Smectite	0.67																										
Albite	5.09	Calcite	0.46																										
Pyrite	2.74	Others	1.63																										
Clay Mineral + Calcareous Ostracodes Lamina	(b ₁) 	(b ₂) 	(b ₃) 	<table><tr><th>Mineral</th><th>Content/%</th><th>Mineral</th><th>Content/%</th></tr><tr><td>Calcite</td><td>31.02</td><td>Apatite</td><td>3.10</td></tr><tr><td>Quartz</td><td>26.21</td><td>Albite</td><td>2.62</td></tr><tr><td>Illite</td><td>17.43</td><td>Pyrite</td><td>2.03</td></tr><tr><td>Chlorite</td><td>7.70</td><td>Smectite</td><td>0.52</td></tr><tr><td>Biotite</td><td>7.25</td><td>Others</td><td>2.12</td></tr></table>	Mineral	Content/%	Mineral	Content/%	Calcite	31.02	Apatite	3.10	Quartz	26.21	Albite	2.62	Illite	17.43	Pyrite	2.03	Chlorite	7.70	Smectite	0.52	Biotite	7.25	Others	2.12	
Mineral	Content/%	Mineral	Content/%																										
Calcite	31.02	Apatite	3.10																										
Quartz	26.21	Albite	2.62																										
Illite	17.43	Pyrite	2.03																										
Chlorite	7.70	Smectite	0.52																										
Biotite	7.25	Others	2.12																										
Clay Mineral + Pyrite Ostracodes Lamina	(c ₁) 	(c ₂) 	(c ₃) 	<table><tr><th>Mineral</th><th>Content/%</th><th>Mineral</th><th>Content/%</th></tr><tr><td>Pyrite</td><td>31.74</td><td>Apatite</td><td>4.62</td></tr><tr><td>Calcite</td><td>21.74</td><td>Biotite</td><td>4.26</td></tr><tr><td>Quartz</td><td>14.55</td><td>Albite</td><td>1.82</td></tr><tr><td>Illite</td><td>9.85</td><td>Smectite</td><td>0.35</td></tr><tr><td>Chlorite</td><td>4.89</td><td>Others</td><td>6.18</td></tr></table>	Mineral	Content/%	Mineral	Content/%	Pyrite	31.74	Apatite	4.62	Calcite	21.74	Biotite	4.26	Quartz	14.55	Albite	1.82	Illite	9.85	Smectite	0.35	Chlorite	4.89	Others	6.18	
Mineral	Content/%	Mineral	Content/%																										
Pyrite	31.74	Apatite	4.62																										
Calcite	21.74	Biotite	4.26																										
Quartz	14.55	Albite	1.82																										
Illite	9.85	Smectite	0.35																										
Chlorite	4.89	Others	6.18																										
Clay Mineral + Ostracodes Fragments Lamina	(d ₁) 	(d ₂) 	(d ₃) 	<table><tr><th>Mineral</th><th>Content/%</th><th>Mineral</th><th>Content/%</th></tr><tr><td>Illite</td><td>36.57</td><td>Chlorite</td><td>5.00</td></tr><tr><td>Quartz</td><td>29.60</td><td>Pyrite</td><td>2.97</td></tr><tr><td>Albite</td><td>7.47</td><td>Apatite</td><td>1.22</td></tr><tr><td>Calcite</td><td>6.43</td><td>K-Feldspar</td><td>0.84</td></tr><tr><td>Biotite</td><td>6.35</td><td>Others</td><td>3.55</td></tr></table>	Mineral	Content/%	Mineral	Content/%	Illite	36.57	Chlorite	5.00	Quartz	29.60	Pyrite	2.97	Albite	7.47	Apatite	1.22	Calcite	6.43	K-Feldspar	0.84	Biotite	6.35	Others	3.55	
Mineral	Content/%	Mineral	Content/%																										
Illite	36.57	Chlorite	5.00																										
Quartz	29.60	Pyrite	2.97																										
Albite	7.47	Apatite	1.22																										
Calcite	6.43	K-Feldspar	0.84																										
Biotite	6.35	Others	3.55																										
Clay Mineral + Felsic Lamina	(e ₁) 	(e ₂) 	(e ₃) 	<table><tr><th>Mineral</th><th>Content/%</th><th>Mineral</th><th>Content/%</th></tr><tr><td>Quartz</td><td>39.15</td><td>Calcite</td><td>5.42</td></tr><tr><td>Illite</td><td>24.49</td><td>Pyrite</td><td>1.93</td></tr><tr><td>Biotite</td><td>8.42</td><td>Smectite</td><td>1.16</td></tr><tr><td>Albite</td><td>7.72</td><td>K-Feldspar</td><td>1.16</td></tr><tr><td>Chlorite</td><td>5.48</td><td>Others</td><td>5.07</td></tr></table>	Mineral	Content/%	Mineral	Content/%	Quartz	39.15	Calcite	5.42	Illite	24.49	Pyrite	1.93	Biotite	8.42	Smectite	1.16	Albite	7.72	K-Feldspar	1.16	Chlorite	5.48	Others	5.07	
Mineral	Content/%	Mineral	Content/%																										
Quartz	39.15	Calcite	5.42																										
Illite	24.49	Pyrite	1.93																										
Biotite	8.42	Smectite	1.16																										
Albite	7.72	K-Feldspar	1.16																										
Chlorite	5.48	Others	5.07																										

Figure 3. Mineral type and composition of different laminar units.

4.2. Clay Mineral–Ostracod Lamina Unit (UB)

The monopolar microscope shows that UB appears as a dark brown base interspersed with bright white bands, with a relatively straight spreading pattern and a thickness distribution of 500 to 2000 µm (Figure 3b₁–d₁). UB consists of three types: the clay mineral–calcareous Ostracod laminar unit (UB₁), the clay mineral–pyrite Ostracod laminar unit (UB₁), and the clay mineral–calcareous Ostracod fragment laminar unit (UB₃) (Figure 3b₁–3d₁). Among these, the intact spindle-shaped Ostracod in UB₁ and UB₂ and the fragmented Ostracod in UB₃ can be seen by SEM (Figure 3b₂–d₂). XRD results indicate that UB has much higher carbonate and pyrite content than both UA and UC (Table 1).

SEM results of UB₁ show that the outer rim of the Ostracod shell is calcite and the inner core is filled with quartz grains, often in association with automorphic pyrite. The organic matter develops in a gap-filling pattern between the outer edge of the shell and the inner core of the Ostracod. In situ mineralogical micro-zone analysis of QEMSCAN also demonstrates that the Ostracod laminae of UB₁ are dominated by calcite and quartz with a high calcite content of 31.02% and quartz content of 26.21% (Figure 3b₃). UB₂ SEM

results reveal that the outer edge of the Ostracod is calcite, and the inner core is densely filled with single pyrite and sphalerite. The organic matter develops in a gap-filling manner in the intergranular pores of pyrite within the Ostracod's core. QEMSCAN results show that the pyrite and calcite contents are 31.73% and 21.74% respectively (Figure 3c₃) and the average TOC content is 2.04%. SEM results of UB₃ show that the Ostracod fragments are semilunar or elongated and form interlayers with the clay in a continuous microwave-like pattern. The thickness of UB₃ is approximately from 100 to 2000 μm . Organic matter is mainly developed in clumps between clay minerals. In combination with QEMSCAN, it can be seen that the calcite content is low compared to UB₁ and UB₂, with illite and quartz dominated (Figure 4b₃).

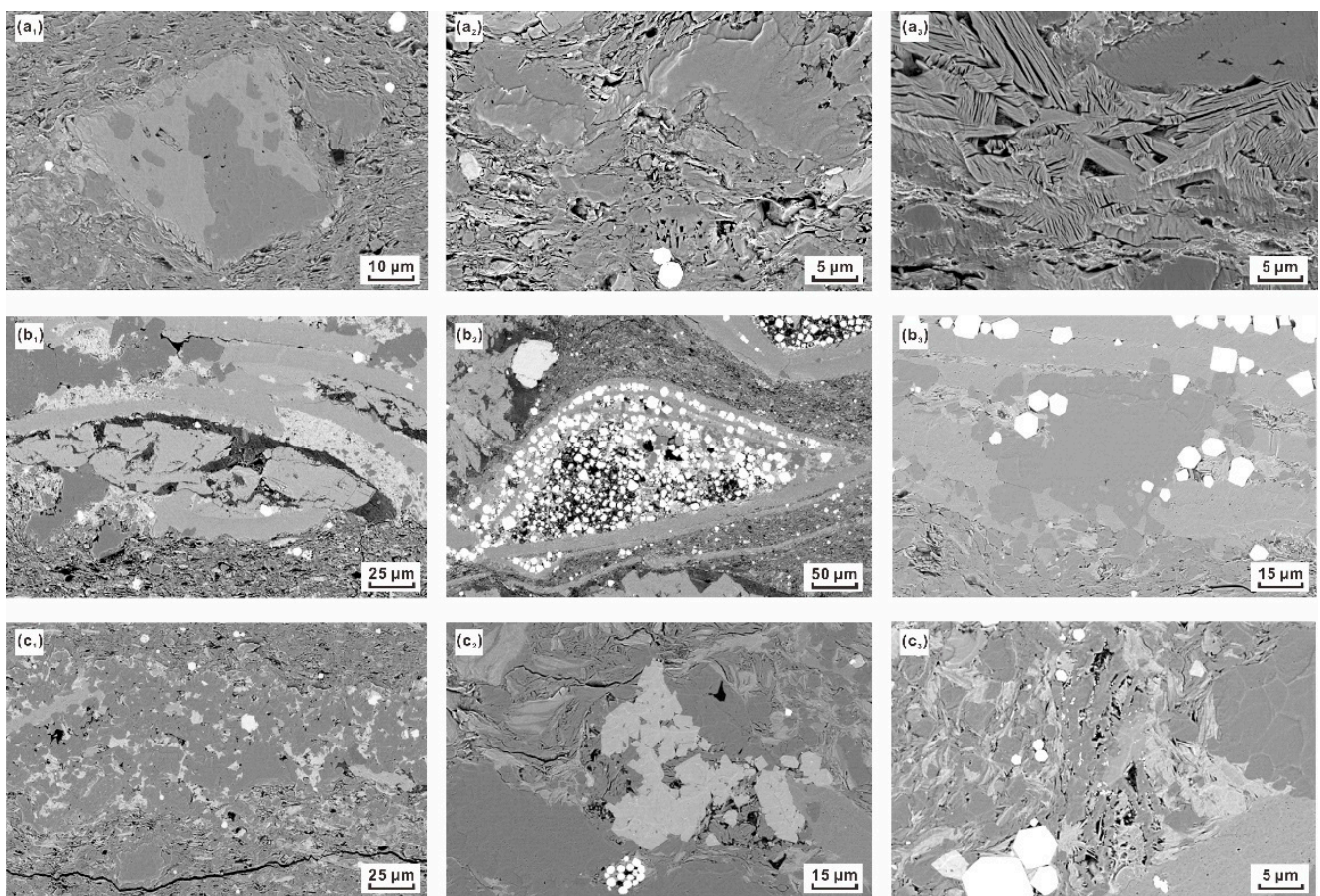


Figure 4. Mineral characteristics and inorganic pore types of the different laminae. (a₁–a₃) are UA, (b₁–b₃) are UB and (c₁–c₃) are UC. (a₁) Calcite dissolved pores and surrounding clay mineral intragranular pores; (a₂) illite intragranular dissolved pores, slit type; (a₃) gypsum intragranular dissolved pores; (b₁) Ostracod shell intergranular pores, shell margin slits, Ostracod shell intragranular dissolved pores and chlorite intragranular pores; (b₂) pyrite intergranular pores; (b₃) clay mineral intergranular pores; (c₁) quartz and albite intergranular pores; (c₂) illite intragranular pores, intergranular pores of illite and quartz; (c₃) chlorite intragranular pores with pyrite developed.

4.3. Clay Mineral-Felsic Laminar Unit (UC)

UC is slightly darker in color under a monopolar microscope, developing continuous horizontal lamina and occasional graded bedding. Its thickness is approximately 50 μm to 200 μm (Figure 3e₁), and the felsic lamina is about 1/6 of the UC (Figure 3e₂). SEM reveals Ostracod fragments, small amounts of mica fragments, pyrite, dolomite, and apatite can develop locally in UC. Quartz and albite are mostly angular and sub-angular in orientation (Figure 3e₂). QEMSCAN shows that the felsic lamina is dominated by quartz and albite at 39.15% and 7.72%, respectively. UC shows a higher quartz and albite content and a lower

clay mineral content than the other units (Figure 3e₃). The average organic carbon content of UC is 2.27%, and the average S1 is 6.72 mg/g (Table 1).

5. Organic-Rich Shale Reservoir Characteristics

In addition to the differences in mineral composition and organic matter content, there are also significant differences in pore types, pore throat networks, and hydrocarbon reservoir space among different types of shale laminae [4,13]. The pore structures of three different laminar units in the Qingshankou Formation of the Gulong Depression were characterized by means of FE-SEM, nitrogen adsorption, FIB-SEM, and nano-CT, and the most favorable laminar combination for shale oil enrichment were compared and selected.

5.1. Reservoir Space of Different Laminar Unit

UA is dominated by intergranular and intragranular pores of clay minerals, which are small in scale. The clay pores are generally slit-like, and the pore diameters range from 500 to 1000 nm. Calcite dissolved pores, gypsum intragranular pores, and pyrite intergranular pores (Figure 4a₁–a₃) are occasionally developed in triangular and irregular shapes, with pore diameters of 1–2 µm. A large number of micro-fractures are developed in the UA, which are distributed along the lamina and extend farther, with widths ranging from 0.5 to 1 µm (Figure 5a₂), which can improve the flow capacity of the shale. Moreover, this type of lamina has high organic carbon and hydrocarbon production potential. Organic matter is mainly produced in agglomerates, including transversely elongated agglomerates, rounded agglomerates, and irregular agglomerates. The size of the agglomerates is highly variable, ranging from 8 to 100 µm. Among these, the pore structure in different types of agglomerates varies. The transversely elongated agglomerates are often associated with microfractures and develop in the same direction as the microfractures. Narrow organic pores of approximately 2 µm in diameter can be often seen within the agglomerates. Occasionally, oil traces can flow and extend along the fractures (Figure 5a₁). The rounded agglomerates have elliptical and triangular pores, which are dense and well connected, with pore diameters ranging from 0.5 to 3 µm (Figure 5a₂). Irregular agglomerates have a flat surface and do not develop organic pores. Their size is generally small, not exceeding 5 µm (Figure 5a₃). UA appears to be one of the important shale oil-rich dominant laminar units.

UB contains three different Ostracod laminae. The reservoir space of UB₁ is dominated by Ostracod shell margin sutures, pyrite intergranular pores, chlorite intragranular pores, and gap-filling organic matter, with occasional intra-shell dissolution pores. The Ostracod shell pores are mainly rounded and micron-sized, with a maximum diameter of 3 µm. The pores in the chlorite grains are mainly slit-type, with a general pore size of fewer than 1 µm and poor connectivity. The filler-like organic matter is mainly developed between the mineral intergranular pores within the Ostracod. Its pore size is small, in the nanometer range. The storage space of UB₂ is dominated by pyrite intergranular pores with large pore space (Figure 4b), in which the filler-like organic matter can be seen to develop. The storage space of UB₃ is dominated by clay mineral-related pores and is blocked by Ostracod fragments. The concomitantly developed clumpy organic matter in UB₃ is identical to the irregular organic matter clumps in UA, with almost no organic pores developed, exhibiting a disadvantaged shale laminar unit (Figure 5b₂).

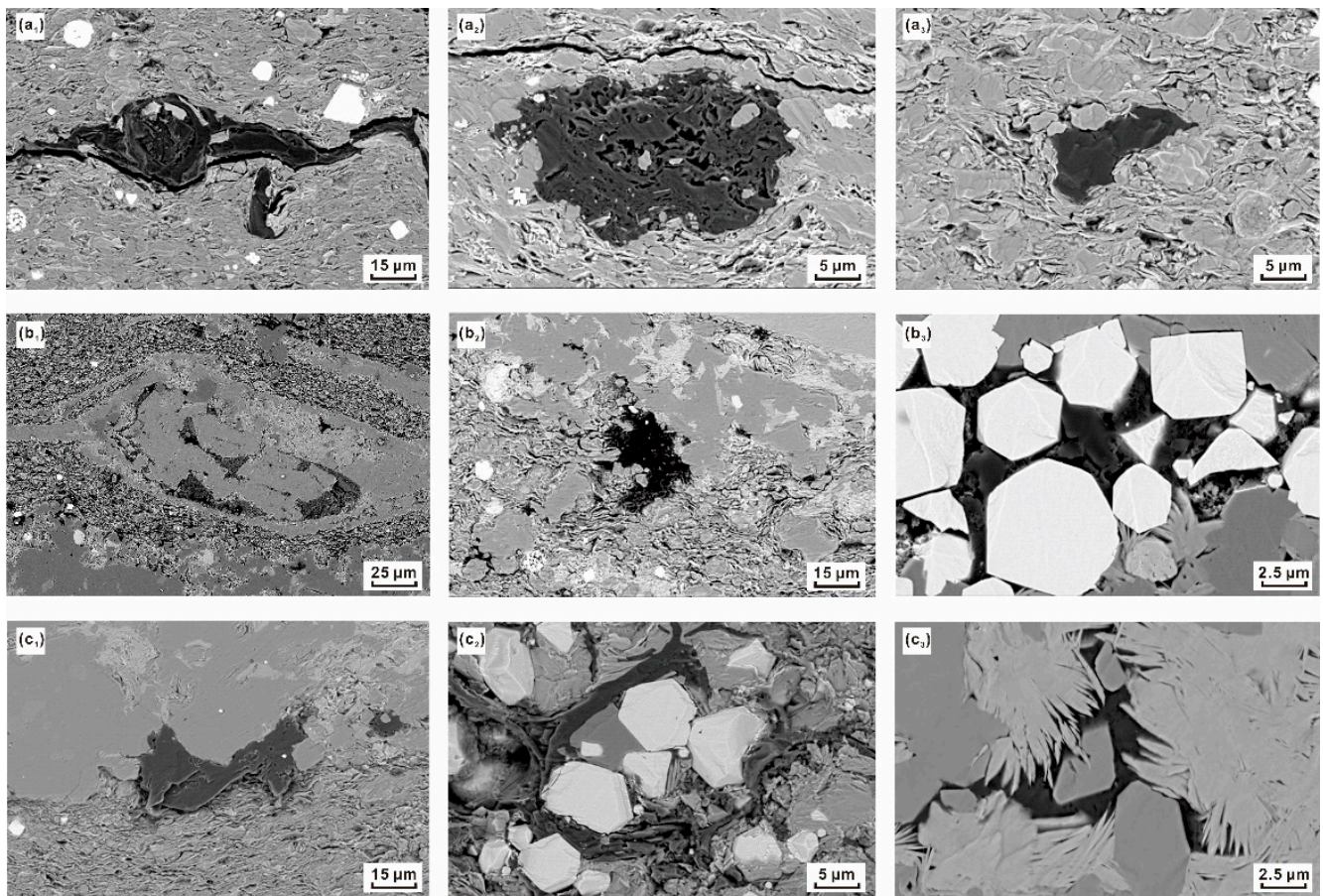


Figure 5. Types and characteristics of organic pores in different laminae. (a₁–a₃) are UA, (b₁–b₃) are UB and (c₁–c₃) are UC. (a₁) Elongate agglomerated organic matter and striated fractures; (a₂) ellipsoidal agglomerated organic matter; (a₃) irregular agglomerated organic matter; (b₁) gap-filling organic matter between Ostracod shells; (b₂) irregular agglomerated organic matter; (b₃) gap-filling organic matter between pyrites; (c₁) irregular organic matter associated with quartz and clay minerals; (c₂) gap-filling organic matter; (c₃) gap-filling organic matter.

UC is dominated by mineral intergranular pores, including brittle mineral intergranular pores and clay mineral intergranular pores (Figure 4c). Intergranular pores of feldspar and quartz grains are commonly filled with illite, black mica, and organic matter (Figure 4c₁). The pores are predominantly micron-sized, up to 5 μm (Figure 4c₁–5c₃). UC mainly develops gap-filling organic matter and irregularly agglomerated organic matter. Among them, the pore size of the gap-filling organic matter is small, between 10 and 100 nm, and grows in the shape of stripes and patterns (Figure 5c₂). The organic matter network is poorly connected because part of the micro and nano pores of gap-filling organic matter can be seen to be covered by illite (Figure 5c₃). Irregularly agglomerated organic matter is associated with quartz and clay minerals, developing honeycomb nanopores (Figure 5c₁).

5.2. Reservoir Properties Evaluation of Different Laminar Units

5.2.1. Nitrogen Adsorption

The low-temperature nitrogen adsorption–desorption isotherms can reflect the pore shape and surface properties of the shale [26]. The experimental results show that the nitrogen adsorption curves of different laminar units are all “S” shaped, but the pore structure of different units is slightly different.

The nitrogen adsorption–desorption curves of UA show that when the relative pressure (P/P_0) is higher than 0.9, the adsorption volume rises rapidly and the desorption line

almost coincides with the adsorption line, reflecting the predominant pore morphology is slit-like (Figure 6). UA mainly develops pores of 15–20 nm, with the presence of pores larger than 25 nm (Figure 6, Table 1). Its pore-specific surface area and specific pore volume are larger than those of UB and UC.

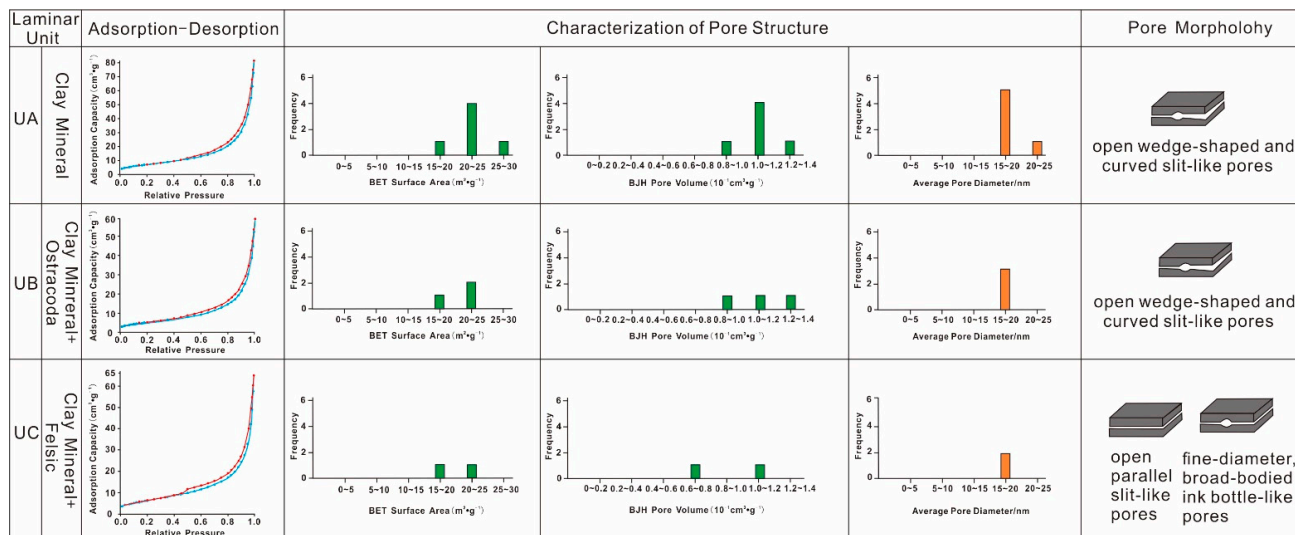


Figure 6. Characterization of the pore structure of nitrogen adsorption.

UB mainly develops open wedge-shaped and curved slit-like pores. Pore diameter, specific surface area and specific pore volume are lower than those for UA. Although Ostracod outer shell rim sutures, Ostracod intershell dissolved pores, pyrite intergranular pores, and chlorite intragranular pores are developed, the pore diameters are generally less than 20 nm.

UC develops fine-diameter, broad-bodied ink-bottle-like pores within the felsic lamina, while parallel slit-like pores develop in the clay minerals laminae. It could be found that the adsorption of UA is greater than UC than UB, which shows that the higher the clay mineral content, the higher the corresponding adsorption amount. The adsorption volumes were obtained by performing a function of nano small-scale pores and specific surface area, indicating that the clay minerals were the main contributors to the pore volume and specific surface area of the selected samples.

5.2.2. D Pore Space Distribution

The space distribution characteristics of the inorganic and organic matter pores of the different laminae were obtained by nano-CT, and the pore connectivity of the organic matter was constructed by FIB-SEM to achieve a three-dimensional reorganization of the pore structure in different laminae. It can be seen that the variability of the pore structure between different laminar units is significant.

The pore diameter, pore volume, and specific surface area of UA are the largest, while UB has the smallest data (Figure 7). The porosity of UA, UB, and UC is 0.97%, 0.32%, and 0.69%, respectively; showing a trend whereby with decreasing content of clay minerals, the porosity decreases. Conversely, the more quartz, calcite, and pyrite are contained, the lower the porosity. This indicates that the clay minerals are the main contributors to the pore space and the presence of brittle minerals is not conducive to pore development.

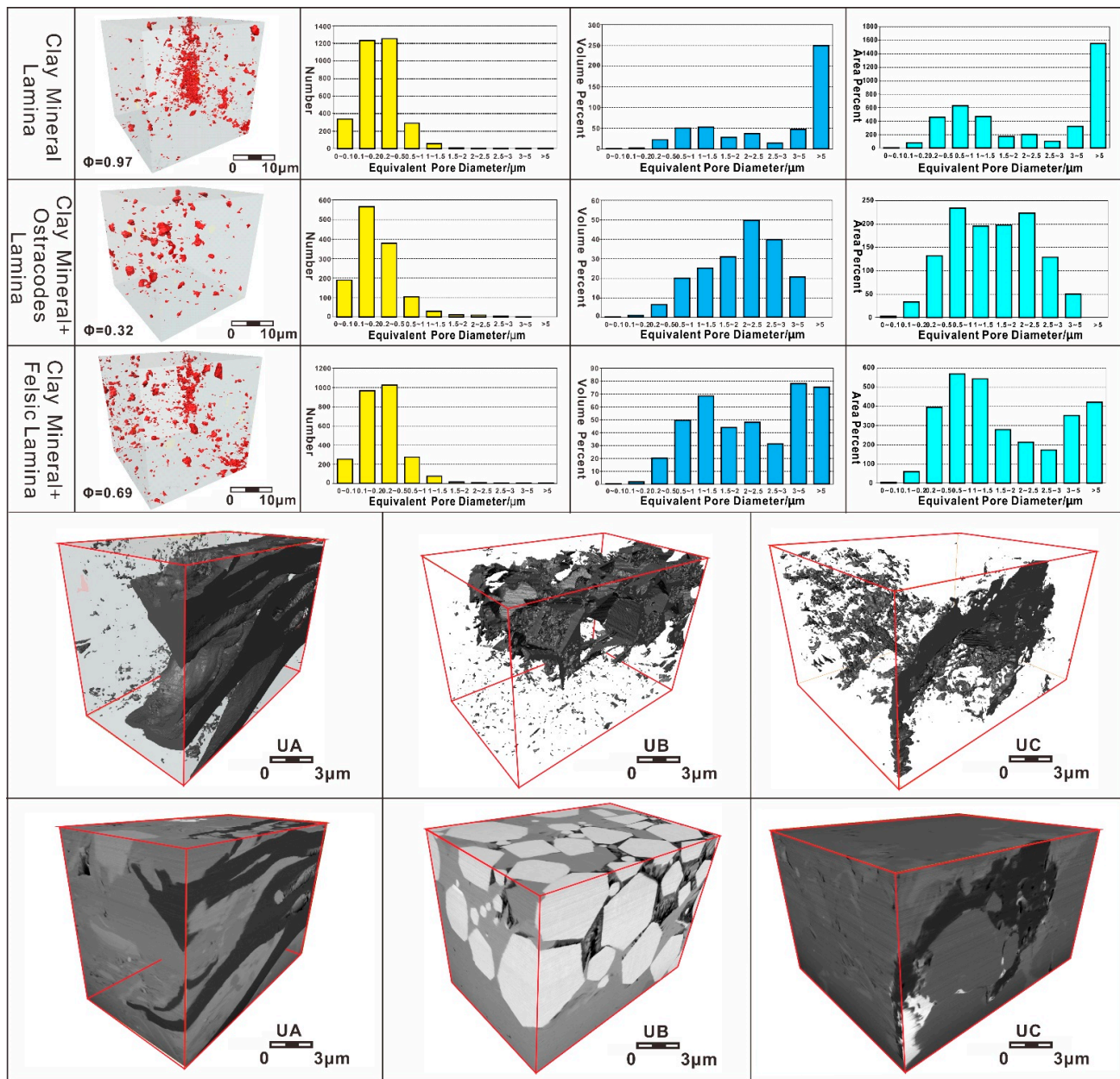


Figure 7. 3D pore characterization of different laminar units.

The distribution of pore volume and specific surface area of UA is a single peak, with the peak corresponding to a pore diameter greater than 5 μm . Although the maximum pore volume and maximum specific surface area of UB samples also correspond to a pore diameter range greater than 5 μm , the values of pore volume and specific surface area of UB samples are relatively small, only 1/5~1/7 those of the UA samples, and the porosity is only 1/3 that of the UA samples. The porosity of the UC sample performs better than UB, but is only 1/2 that of UA, with a twin peak distribution of pore volume and specific surface area. The peak pore sizes are mainly concentrated within 0.5 μm ~1.5 μm or greater than 3 μm .

6. Discussion

The pore structure of shale reservoirs is the result of both hydrocarbon generation of organic matter and diagenetic evolution [27]. The organic acid dissolution accompanied by the organic matter hydrocarbon generation process, the transformation of clay minerals,

and calcareous cementation under different degrees of thermal evolution degree are the keys to the differences in pore structure in different laminae.

6.1. Thermal Evolution Degree

The UA is known to have the highest content of clay minerals in the study area, and its specific pore volume, specific surface area, pore radius, and porosity perform the best, indicating that clay minerals are the main contributors to the pore space of the shales in the Qingshankou Formation of the Gulong Depression, and the clay mineral lamina is one of the most important shales oil-rich dominant laminar units. This conclusion differs from the Yanchang Formation of the Ordos Basin and the Luchaogou Formation of the Junggar Basin, where the higher the clay mineral content, the worse the shale's physical properties [16,28]. Because of the high Ro of the Qingshankou Formation, is greater than 1.0% and up to 1.6% [17], which is higher than that of the Yanchang Formation and the Luchaogou Formation (Ro between 0.7%–1.0%). The clay-mineral lamina of the Qingshankou Formation is dominated by illite, with mainly narrow-type sutured intergranular pores and microfractures developed, the pore channels are better than other laminar units, while the clay mineral lamina in the low-maturity area is dominated by illite/smectite mixed layer, with limited development of intergranular pores and microfractures. Therefore, the authors believe that the thermal evolutionary degree is an important factor influencing the clay mineral laminae of the maturity study area to be the dominant laminar unit.

6.2. Clay Mineral Transformations

XRD and SEM results could reveal that the clay minerals of the shale samples are dominated by illite and illite/smectite mixed layers, and the samples contain much microcrystalline quartz and albite, but less potassium feldspar (Figure 3). This phenomenon suggests that there is a process, whereby montmorillonite precipitates silica and consumes large amounts of potassium ions to convert to illite (Figure 8c). During the conversion process the water molecules between the montmorillonite layers are gradually expelled and the thickness of the mineral monolayer decreases, producing high pressure and horizontally oriented micro-fractures. The phenomenon of relatively abundant micro-fractures developing within the clay minerals can be verified in the SEM results (Figure 4). These micro-fractures can increase the effectiveness and connectivity of the pores within the clay mineral lamina to some extent, improving the storage capacity of shale [29].

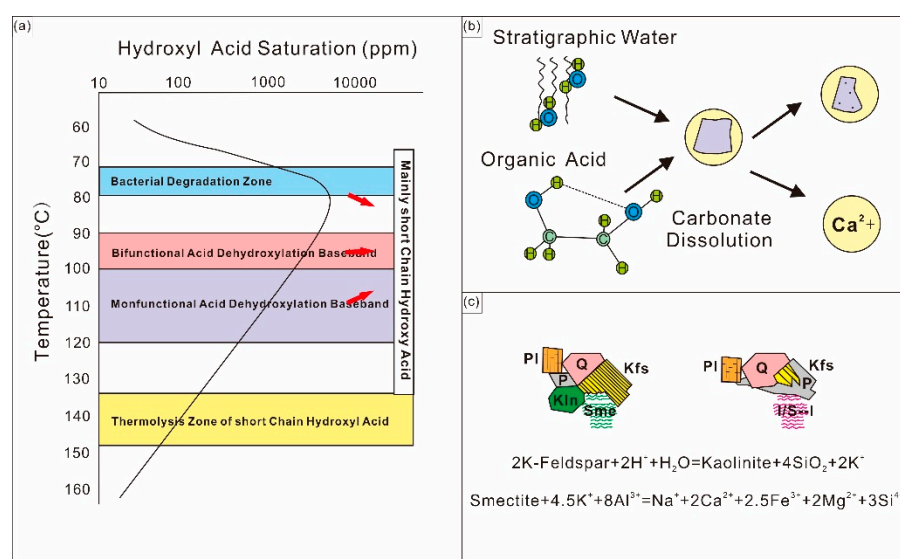


Figure 8. Diagenetic influences on different laminae. (a) the variation of hydroxyl acid saturation at different temperature, (b) the reaction between carbonate minerals and organic acid; (c) the process of transforming from montmorillonite to illite.

6.3. Carbonate Cementation and Organic Acid Dissolution

The early sedimentation of pore-filling carbonate can increase the compressive capacity of the reservoir and provide opportunities for subsequent dissolution [30], while the late sedimentation of carbonate cement can reduce the final porosity. Therefore, the timing of precipitation, dissolution, and distribution of carbonate cement has an important impact on reservoir quality. In UB and UC, carbonate minerals are found to be cemented around the Ostracod shell and quartz grains in long and irregular forms, respectively, blocking the primary pores. At the same time, the development of secondary pores in the laminar units correlates less with calcite dissolved pores and more with Ostracod shell rim joints, pyrite intergranular pores, and chlorite intra-granular pores (Figure 4b₃). This anomaly occurs because when the burial depth exceeds 2500 m, the shales of the Qingshankou Formation in the Gulong Depression are at a low concentration of organic acid discharge (Figure 8a) and are unable to produce large amounts of short-chain hydroxyl acids [31] to form secondary dissolved pores by dissolution reactions with labile minerals such as potassium feldspar, albite, and calcite cement (Figure 8b). As a result, calcite cement is more developed in shale reservoirs in the study area than in others. In addition, it can fill primary intergranular pores and fractures and act as a disruption to the reservoir space, resulting in inferior reservoir properties in the UB and UC compared to the UA.

6.4. Development Patterns of Different Laminar Units

To further explore the influence of the development of different laminae reservoir qualities from a microscopic perspective, the “source” (S1, oil transcendence index and total organic carbon content), and “reservoir” (mineral type, fracture, pore morphology, BJH specific pore volume, BET specific surface area and porosity) are characterized and spatially matched to establish reservoir development patterns for different laminae in high-clay-mineral shales (Figure 9).

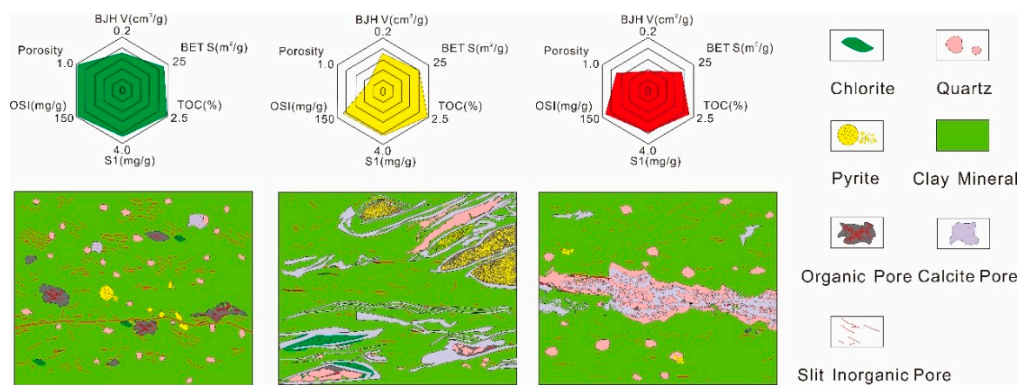


Figure 9. Distribution of mineral composition, reservoir, and oil-bearing patterns for different laminae.

UA has high organic matter abundance and hydrocarbon generation potential, and the transformation stage of the illite/smectite mixed layer to illite is prone to the generation of more intergranular pores and microfractures [32–34], so the liquid hydrocarbons generated during peak oil generation can be transported to the nearby inorganic pores for preservation, which is conducive to the formation of a well-matched “source-storage” pattern. In contrast, UB has a higher carbonate content and lower organic matter content than UA, resulting in a reduced contribution of organic matter pores to the total porosity. The UB “source-storage” model is considered inferior to UA, in combination with the calcium-rich cementation and pore plugging by pyrite. The organic matter content of UC is also low, and the organic matter is mainly homogeneous and massive, with a low degree of organic matter pore development. In combination with the calcareous cement commonly found in the felsic lamina, they block the intergranular pores of the clay minerals, thus reducing the pore connectivity. The “source-storage” model of the UC is therefore also inferior to that of UA.

7. Conclusions

Combined with XRF, XRD, Rock-Eval, FE-SEM, QEMSCAN, N₂ adsorption tests, nano CT and other methods, the mineral composition and pore structure characteristics of different laminar units of high-clay shale samples from the Qingshankou Formation in Songliao Basin were studied. The classification of different laminar units and their corresponding reservoir quality information were determined, and the pore information (pore volume, pore area, and pore size distribution) and three-dimensional pore connectivity were discussed in detail. The following conclusions can be drawn:

1. Three types of laminae are mainly developed in the high-clay shale of the Qingshankou Formation in Gulong Depression, Songliao basin. These include clay mineral lamina, Ostracod lamina, and felsic lamina. Among them, the Ostracod lamina can be divided into calcareous Ostracod lamina, pyrite Ostracod lamina, and Ostracod fragment lamina. Three kinds of laminar units are formed: UA (clay mineral lamina), UB (clay mineral–Ostracod lamina), and UC (clay mineral–felsic lamina).
2. FE-SEM shows that the pore structures of different laminar units are significantly different. UA reservoir space is mainly composed of intergranular and intragranular pores of clay minerals, fractures, and organic pores. UB reservoir space is dominated by Ostracod shell margin sutures and intershell dissolved pores, pyrite intergranular pores, and chlorite intragranular pores; UC mainly develops intragranular pores of albite, chlorite and illite. The results of nitrogen adsorption, nano CT and FIB-SEM characterize the pore size distribution of different scales. It is found that UA mainly develops 15~20 nm slit-like pores, UB develops open wedge-shaped and curved slit-like pores, UC develops ink bottle-like pores with a fine diameter and wide body inside the felsic lamina, while parallel slit-like pores develop in the clay minerals.
3. Comparing the 3D pore reconstruction images of different laminae and the porosity obtained by nano-CT, FIB-SEM, and NMR, it is found that the clay mineral laminae in the study area are the laminae with the highest porosity, and its specific pore volume, specific surface area, pore radius, and porosity are the best.
4. Through the comparison of samples from different basins, it is found that the main reasons for the existence of physical differences between different laminae are the effects of the thermal evolution degree and diagenesis. At high maturity, the conversion of montmorillonite to illite in the UA increases the connectivity of pores within the clay mineral lamina. Meanwhile, the supply of organic acids in the UB and UC is insufficient, and the calcareous cementation tends to lead to pore blockage, resulting in 3~7 times more pore volume in the UA than in the UB and UC. In the future, we will conduct further research on shale with different maturity, and discuss in detail the difference between laminae caused by the effect of maturity on shale diagenesis evolution.

Author Contributions: G.H.: Conceptualization, Methodology, Writing—Original draft preparation; S.W.: Supervision, Writing—Review and Editing, Validation; J.Z.: Resources, Validation; R.L., M.G.: Data Curation; Y.C., M.L.: Validation; S.Z.: Validation. All authors have read and agreed to the published version of the manuscript.

Funding: This research was funded by the National Natural Science Foundation of China (42072187) and R&D Department of China National Petroleum Corporation (2021DQE-0405).

Institutional Review Board Statement: Not applicable.

Informed Consent Statement: Not applicable.

Data Availability Statement: The data presented in this study are available on request from the corresponding author.

Conflicts of Interest: The authors declare no conflict of interest.

References

1. Zou, C.; Yang, Z.; Cui, J.; Zhu, R.; Hou, L.; Tao, S.; Yuan, X.; Wu, S.; Lin, S.; Wang, L.; et al. Formation mechanism, geological characteristics and development strategy of nonmarine shale oil in China. *Pet. Explor. Dev.* **2013**, *40*, 14–26. [\[CrossRef\]](#)
2. Sun, L. Gulong shale oil (preface). *Pet. Geol. Oilfield Dev. Daqing* **2020**, *39*, 1–7.
3. Wang, Y.; Liang, J.; Zhang, J.; Zhao, B.; Zhao, Y.; Liu, X.; Xia, D. Resource potential and exploration direction of Gulong shale oil in Songliao Basin. *Pet. Geol. Oilfield Dev. Daqing* **2020**, *39*, 20–34.
4. Lin, S.; Yuan, X.; Yang, Z. Comparative study on lacustrine shale and mudstone and its significance: A case from the 7th member of Yanchang Formation in the Ordos Basin. *Oil Gas Geol.* **2017**, *38*, 517–523.
5. Jin, Z.; Wang, G.; Liu, G.; Gao, B.; Liu, Q.; Wang, H.; Liang, X.; Wang, R. Research progress and key scientific issues of continental shale oil in China. *Acta Pet. Sin.* **2021**, *42*, 15.
6. Jarvie, D. Shale resource systems for oil and gas: Part 2—Shale-oil resource systems. In *Shale Reservoirs—Giant Resources for the 21st Century: AAPG Memoir 97*; Breyer, J.A., Ed.; The American Association of Petroleum Geologists: Tulsa, OK, USA, 2012; pp. 89–119.
7. Yawar, Z.; Schieber, J. On the origin of silt laminae in laminated shales. *Sediment. Geol.* **2017**, *360*, 22–34. [\[CrossRef\]](#)
8. Hua, G.; Wu, S.; Qiu, Z.; Jing, Z.; Xu, J.; Guan, M. Lamination Texture and Its Effect on Reservoir Properties: A Case Study of Longmaxi Shale, Sichuan Basin. *Acta Sedimentol. Sin.* **2021**, *39*, 16.
9. Rokosh, D.; Pawlowicz, J.; Anderson, S.; Berhane, M.; Beaton, A. Shale fabric, mineralogy and effective porosity of the upper Colorado group. In *Frontiers + Innovation*; Alberta CSPG CSEG CWLS Convention: Calgary, AB, Canada, 2009; pp. 572–576.
10. Sutton, S.; Ethridge, F.; Almon, W.; Dawson, W.; Edwards, K. Textural and sequence-stratigraphic controls on sealing capacity of Lower and Upper Cretaceous shales, Denver basin, Colorado. *AAPG Bull.* **2004**, *88*, 1185–1206. [\[CrossRef\]](#)
11. Slatt, R.; O'Brien, N. Pore types in the Barnett and Woodford gas shales: Contribution to understanding gas storage and migration pathways in fine-grained rocks. *AAPG Bull.* **2011**, *95*, 2017–2030. [\[CrossRef\]](#)
12. Brittenham, M. Geologic analysis of the upper Jurassic Haynesville shale in East Texas and West Louisiana: Discussion. *AAPG Bull.* **2013**, *97*, 525–528. [\[CrossRef\]](#)
13. Huang, Z.; Liu, G.; Li, T.; Li, Y.; Yin, Y.; Wang, L. Characterization and control of mesopore structural heterogeneity for low thermal maturity shale: A case study of yanchang formation shale, ordos basin. *Energy Fuels* **2017**, *31*, 11569–11586. [\[CrossRef\]](#)
14. Breyer, J.; Denne, R.; Kosanke, T.; Spaw, J.; Funk, J.; Christianson, P.; Bush, D.A.; Nelson, R.A. Facies, Fractures, Pressure and Production in the Eagle Ford Shale (Cretaceous) between the Maverick Basin and the San Marcos Arch, Texas, USA. In *Proceedings of the Unconventional Resources Technology Conference*, San Antonio, TX, USA, 1–3 August 2016.
15. Zhao, K. *Characteristics and Genesis of Carbonate Laminae in the Upper Es4-Es3 Lower Member of Dongying Sag, Bohai Bay Basin*; China University of Geosciences: Wuhan, China, 2019.
16. Xi, K.; Li, K.; Cao, Y.; Lin, M.; Niu, X.; Zhu, R.; Wei, X.; You, Y.; Liang, X.; Feng, S. Laminae combination and shale oil enrichment patterns of Chang 73 sub-member organic-rich shales in the Triassic Yanchang Formation, Ordos Basin, NW China. *Pet. Explor. Dev.* **2020**, *47*, 1342–1353. [\[CrossRef\]](#)
17. Sun, L.; Liu, H.; He, W.; Li, G.; Zhang, S.; Zhu, R.; Jin, X.; Meng, S.; Jiang, H. An analysis of major scientific problems and research paths of Gulong shale oil in Daqing Oilfield, NE China. *Pet. Explor. Dev.* **2021**, *48*, 527–540. [\[CrossRef\]](#)
18. Liu, B.; Shi, J.; Fu, X.; Lv, Y.; Sun, X.; Gong, L.; Bai, Y. Petrological characteristics and shale oil enrichment of lacustrine fine-grained sedimentary system: A case study of organic-rich shale in first member of Cretaceous Qingshankou Formation in Gulong Sag, Songliao Basin, NE China. *Pet. Explor. Dev.* **2018**, *45*, 828–838. [\[CrossRef\]](#)
19. Wu, H.; Lin, T.; Bai, Y.; Zhang, J.; Liu, X.; Huo, Q.; Zhang, Y.; Li, J. Analyses of the mudstone (shale) oil exploration potential in North Songliao Basin. *Pet. Geol. Oilfield Dev. Daqing* **2019**, *38*, 78–86.
20. Zhang, J.; Xu, X.; Bai, J.; Liu, W.; Chen, S.; Liu, C.; Li, Y. Enrichment and exploration of deep lacustrine shale oil in the first Member of Cretaceous Qingshankou Formation, southern Songliao Basin, NE China. *Pet. Explor. Dev.* **2020**, *47*, 637–652. [\[CrossRef\]](#)
21. Subcommittee 3 on Geology Exploration of National Technical Committee 355 on Petroleum of Standardization Administration of China. In *The Determination of Total Organic Carbon in Sedimentary Rocks*; GB/T 19145-2003; China Quality and Standards Publishing&Media CO., Ltd.: Beijing, China, 2003; pp. 1–2.
22. Subcommittee 3 on Geology Exploration of National Technical Committee 355 on Petroleum of Standardization Administration of China. In *Rock Pyrolysis Analysis*; GB/T 18602-2001; China Quality and Standards Publishing&Media CO., Ltd.: Beijing, China, 2002; pp. 1–5.
23. Subcommittee 3 on Geology Exploration of National Technical Committee 355 on Petroleum of Standardization Administration of China. In *Analysis Method for Clay Minerals and Ordinary Non-Clay Minerals in Sedimentary Rocks by the X-ray Diffraction*; SY/T 5163-2010; Petroleum Industry Press: Beijing, China, 2010; pp. 1–43.
24. Wu, S.; Lin, S.; Chao, D.; Zhai, X.; Wang, X.; Huang, X.; Xu, J. Fluid mobility evaluation based on pore structure investigation in tight sandstones: Case study of Upper Triassic Chang 6 tight sandstones in Huaqing area, Ordos Basin. *Nat. Gas Geosci.* **2019**, *30*, 1222–1232.
25. Subcommittee 3 on Geology Exploration of National Technical Committee 355 on Petroleum of Standardization Administration of China. In *3D Pore Structure Characterization of Rocks—Part 1: CT Scanning Method*; SY/T 7410.1-2018; Petroleum Industry Press: Beijing, China, 2010; pp. 1–43.

26. Shan, C.; Zhang, T.; Guo, J.; Zhang, Z.; Yang, Y. Characterization of the micropore systems in high-rank coal reservoirs of the southern Sichuan Basin, China. *AAPG (Am. Assoc. Pet. Geol.) Bull.* **2015**, *99*, 2099–2119. [[CrossRef](#)]
27. Aplin, A.C.; Macquaker, J. Mudstone diversity: Origin and implications for source, seal and reservoir properties in petroleum systems. *AAPG Bull.* **2011**, *95*, 2031–2059. [[CrossRef](#)]
28. Wang, J.; Zhou, L.; Jin, J.; Liu, J.; Chen, J.; Jiang, H.; Zhang, B. Pore structure, hydrocarbon occurrence and their relationship with shale oil production in Lucaogou Formation of Jimsar Sag, Junggar Basin. *Pet. Geol. Exp.* **2021**, *43*, 941–948.
29. Li, Y.; Cai, J. Effect of smectite illitization on shale gas occurrence in argillaceous source rocks. *Pet. Geol. Exp.* **2014**, *36*, 352–358.
30. Morad, S. Carbonate Cementation in Sandstones | Calcite Cement in Shallow Marine Sandstones. In *Growth Mechanisms and Geometry*; Blackwell Science: Hoboken, NJ, USA, 1998. [[CrossRef](#)]
31. Surdam, R.C.; Crossey, L.J.; Hagen, E.S.; Heasler, H.P. Organic-inorganic interactions and Sandstone diagenesis. *Amer. Assoc. Pet. Geol. Bull.* **1989**, *73*, 1–23.
32. Bai, C.; Yu, B.; Liu, H.; Xie, Z.; Han, S.; Zhang, L.; Ye, R.; Ge, J. The genesis and evolution of carbonate minerals in shale oil formations from Dongying depression, Bohai Bay Basin, China. *Int. J. Coal Geol.* **2018**, *189*, 8–26. [[CrossRef](#)]
33. Wang, M.; Chen, Y.; Song, G.; Steele-Macinnis, M.; Liu, Q.; Wang, X.; Zhang, X.; Zhao, Z.; Liu, W.; Zhang, H. Formation of bedding-parallel, fibrous calcite veins in laminated source rocks of the Eocene Dongying Depression: A growth model based on petrographic observations. *Int. J. Coal Geol.* **2018**, *200*, 18–35. [[CrossRef](#)]
34. Aldega, L.; Carminati, E.; Scharf, A.; Mattern, F. Thermal maturity of the Hawasina units and origin of the Batinah Mélange (Oman Mountains): Insights from clay minerals. *Mar. Pet. Geol.* **2021**, *133*, 105316. [[CrossRef](#)]